International Journal of Hydrogen Energy 211 (2026) 153663

Contents lists available at ScienceDirect

International Journal of Hydrogen Energy

journal homepage: www.elsevier.com/locate/he

First-principles study of structural, elastic, electronic, optical, thermodynamic, phonon, and hydrogen storage properties of XMg_2H_5 (X =Li, Na, K)

Salih Ermiş [a], Sümeyra Yamçıçıer [b], Cihan Kürkçü [c,*]

[a] Department of Electrical-Electronic Engineering, Kırşehir Ahi Evran University, Kırşehir, Türkiye
[b] Department of Medical Services and Techniques, Osmaniye Korkut Ata University, Osmaniye, Türkiye
[c] Department of Electronics and Automation, Kırşehir Ahi Evran University, Kırşehir, Türkiye

ARTICLE INFO

Keywords:
Hydrogen storage
Structural
Electronic
Elastic
Optical
Thermodynamic

ABSTRACT

First-principles density functional theory calculations were performed to investigate the structural, elastic, electronic, optical, thermodynamic, and hydrogen storage properties of $LiMg_2H_5$, $NaMg_2H_5$, and KMg_2H_5 compounds. All structures crystallize in the orthorhombic *Pmmn* phase and exhibit negative formation energies (−0.207, −0.183, and −0.242 eV), indicating thermodynamic stability. The calculated bulk and shear moduli are 45.27 and 35.22 GPa for $LiMg_2H_5$, 22.48 and 19.53 GPa for $NaMg_2H_5$, and 36.63 and 26.67 GPa for KMg_2H_5, revealing strong interatomic bonding and mechanical stability. The corresponding Poisson's ratios (0.19–0.24) confirm brittle elastic behavior. The electronic band gaps are 2.97 eV for $LiMg_2H_5$, 3.07 eV for $NaMg_2H_5$, and 2.76 eV for KMg_2H_5, verifying their semiconducting character, which is suitable for hydrogen-related applications. Optical analysis indicates pronounced interband transitions in the ultraviolet region with plasmon peaks around 9–12 eV. The Debye temperatures obtained from thermodynamic analysis are 807.62 K, 547.98 K, and 588.16 K, respectively, implying stable lattice dynamics. The theoretical gravimetric hydrogen capacities are 8.32 wt%, 6.58 wt%, and 5.43 wt%, with corresponding desorption temperatures of 152.47 K, 135.14 K, and 178.59 K. These results provide detailed insight into the structural stability, mechanical hardness, electronic nature, and hydrogen storage potential of Mg-based hydrides.

1. Introduction

The growing concerns over global warming, depletion of fossil fuel reserves, and environmental degradation have intensified the search for sustainable and clean energy sources. Among various renewable alternatives, hydrogen has emerged as one of the most promising energy carriers due to its high energy density (142 MJ kg^{-1}), carbon-free combustion product, and suitability for integration into diverse energy systems such as fuel cells, hybrid vehicles, and grid-scale storage [1–5]. Unlike conventional fossil fuels, hydrogen combustion generates only water as a byproduct, making it an environmentally benign solution for reducing greenhouse gas emissions and mitigating climate change. However, the safe and efficient storage of hydrogen remains one of the major technological challenges that hinder its widespread utilization in practical energy applications [6,7]. Hydrogen can be stored in gaseous, liquid, or solid forms. Although gaseous and cryogenic liquid storage methods are technologically mature, they suffer from serious disadvantages such as low volumetric density, high pressure requirements, and severe safety concerns. In contrast, solid-state hydrogen storage materials, particularly metal and complex hydrides, have gained great attention due to their high volumetric and gravimetric capacities, good reversibility, and inherent safety [8–10]. Metal hydrides can store hydrogen through reversible chemical bonding between metal atoms and hydrogen, providing a compact and safe storage medium compared to compressed or liquid hydrogen systems. Among the known hydride families, magnesium-based hydrides (MgH_2, Mg_2MH_6, and related compounds) have attracted considerable research interest because of their low cost, abundance, light weight, and relatively high hydrogen content (up to 7.6 wt%) [11–13]. However, pure MgH_2 suffers from sluggish hydrogen absorption/desorption kinetics, as well as a high decomposition temperature (~573 K), which limits its practical application. Therefore, various strategies such as alloying, doping, and

* Corresponding author.
E-mail addresses: sermis@ahievran.edu.tr (S. Ermiş), sumeyrayamcicier@osmaniye.edu.tr (S. Yamçıçıer), ckurkcu@ahievran.edu.tr (C. Kürkçü).

https://doi.org/10.1016/j.ijhydene.2026.153663
Received 2 November 2025; Received in revised form 9 January 2026; Accepted 22 January 2026
Available online 28 January 2026

substitution with alkali or transition metals have been proposed to improve the thermodynamic stability and hydrogen release characteristics of Mg-based systems [14–16]. In recent years, complex hydrides composed of alkali (Li, Na, K) and alkaline-earth (Mg, Ca) metals have emerged as a new class of hydrogen storage materials exhibiting tunable thermodynamic and structural properties [17–19]. These hydrides typically feature mixed ionic–covalent bonding environments, allowing modification of hydrogen binding energies through cation substitution. For instance, $LiMgH_3$, $LiMg_2H_5$, and Li_2MgH_4 systems have been reported to possess high hydrogen capacities and relatively lower desorption enthalpies compared to MgH_2, indicating enhanced reversibility and kinetics [20]. Na- and K-substituted counterparts, such as $NaMg_2H_5$ and KMg_2H_5, are of particular interest because the larger ionic radii of Na^+ and K^+ can expand the lattice, weaken metal–hydrogen bonding, and consequently facilitate hydrogen desorption at lower temperatures [21]. Experimental and computational studies have shown that the thermodynamic and mechanical stability of these compounds strongly depend on the type of alkali metal involved, which controls both lattice parameters and hydrogen diffusion pathways [21–23].

Abdellaoui et al. [24] investigated the effect of substituting light elements such as boron (B) and lithium (Li) into MgH_2 and demonstrated that dual substitution (in the Mg_4BLiH_{12} compound) significantly improves the storage performance. The modified system achieved a gravimetric capacity of 9.45 wt% and a volumetric capacity of 123 g H_2 L^{-1}, surpassing pure MgH_2, while simultaneously lowering the desorption temperature due to weakened Mg–H bonding, thereby enhancing the hydrogen release kinetics. In parallel, Gao et al. [25] provided a comprehensive review of Li/Mg-based hydrides for both hydrogen and lithium storage applications, highlighting remarkable progress in catalytic design, thermodynamic tuning, nanostructuring, and external field-assisted techniques. Their study emphasized that optimizing ion transport pathways and improving structural stability through advanced modification strategies can significantly enhance ionic conductivity, reversibility, and overall storage efficiency, positioning Li/Mg hydrides as promising candidates for next-generation high-energy storage systems. Complementing these findings, Moharam et al. [26] conducted first-principles (DFT) simulations on $XMgNiH_4$ (X = Ba, Li) compounds and reported hydrogen storage capacities ranging from 6.2 wt% to 7.7 wt%, along with negative formation energies and semiconducting behavior. Their electronic structure analysis revealed hybridization between Ni-d and H-s/p orbitals, contributing to the structural stability and hydrogen binding strength of these hydrides These findings indicate that alkali-metal substitution in Mg-based hydrides offers a promising route for optimizing both thermodynamic and mechanical properties for hydrogen storage applications. However, a comprehensive understanding of the structure–property–hydrogen storage relationship in XMg_2H_5 (X = Li, Na, K) systems is still limited. Most previous works have focused either on thermodynamics or on electronic structure alone, without providing a detailed correlation among their elastic, electronic, optical, and thermal characteristics.

To bridge this gap, the present study employs first-principles density functional theory (DFT) calculations to provide a holistic understanding of the structural, elastic, electronic, optical, thermodynamic, and hydrogen storage properties of $LiMg_2H_5$, $NaMg_2H_5$, and KMg_2H_5 compounds. The orthorhombic *Pmmn* phase of these hydrides is systematically analyzed to reveal how the substitution of alkali metals affects the bonding environment, stability, mechanical behavior, and hydrogen release mechanisms. Elastic constant analysis is conducted to evaluate mechanical stability and ductility, which are critical for cyclic hydrogen absorption/desorption operations. Electronic band structure and density of states (DOS) calculations are performed to determine the nature of chemical bonding and to assess the semiconducting characteristics that can influence charge transport during hydrogenation. Optical functions such as dielectric response, reflectivity, and energy-loss spectra are investigated to explore photon–electron interactions and potential applications in optical sensing and diagnostics. Additionally, thermodynamic parameters including Debye temperature, melting point, and minimum thermal conductivity are derived to understand lattice dynamics and heat transport properties. Finally, the theoretical gravimetric and volumetric hydrogen capacities are calculated to assess the potential of these hydrides in meeting the U.S. Department of Energy (DOE) targets for 2025. Through these comprehensive analyses, this study aims to (i) clarify the influence of alkali-metal substitution on the structural stability and bonding nature of Mg-based hydrides, (ii) correlate mechanical stiffness and anisotropy with hydrogen absorption/desorption reversibility, (iii) explore the electronic and optical signatures associated with hydrogen–metal interactions, and (iv) evaluate their thermodynamic feasibility and storage performance under practical conditions. By systematically comparing Li-, Na-, and K-based Mg_2H_5 compounds, this work not only elucidates the fundamental mechanisms governing their stability and hydrogen storage capability but also provides valuable theoretical guidance for designing next-generation lightweight hydrogen storage materials with optimized thermodynamic and mechanical characteristics. The findings are expected to serve as a reference framework for future experimental and computational efforts focused on tailoring complex hydrides for sustainable hydrogen energy technologies [14,27].

In contrast to previous studies that primarily focus on isolated properties of magnesium-based hydrides, this work provides a comprehensive and systematic first-principles investigation of the XMg_2H_5 (X = Li, Na, K) series in the orthorhombic *Pmmn* phase. The primary novelty of this research lies in its holistic approach, integrating thermodynamic stability and phonon dynamics with a highly detailed analysis of elastic anisotropy and frequency-dependent optical responses aspects that have remained largely unexplored for these specific compounds. Our findings reveal that all investigated materials exhibit exceptional gravimetric hydrogen storage capacities: 8.32 wt% for $LiMg_2H_5$, 6.58 wt% for $NaMg_2H_5$, and 5.43 wt% for KMg_2H_5. Notably, both $LiMg_2H_5$ and $NaMg_2H_5$ clearly surpass the U.S. Department of Energy (DOE) 2025 target of 5.5 wt%, while KMg_2H_5 remains highly competitive, meeting the requirements for high-capacity solid-state storage. Furthermore, the establishment of a direct correlation between alkali-metal substitution and directional mechanical integrity provides a crucial theoretical benchmark for predicting the structural durability of these hydrides during long-term hydrogen absorption/desorption cycling. By situating these multi-physical properties within a comparative framework, this study fills a significant gap in the literature and offers vital insights for the design of next-generation, high-capacity, and mechanically robust hydrogen storage materials.

2. Calculation methods

All first-principles calculations were performed within the framework of density functional theory (DFT) using the CASTEP program [28]. The exchange–correlation interactions were treated using the generalized gradient approximation (GGA) with the Perdew–Burke–Ernzerhof (PBE) functional [29]. The structural optimizations were carried out employing the Broyden–Fletcher–Goldfarb–Shanno (BFGS) algorithm [30] until the convergence criteria were satisfied. A plane-wave energy cutoff of 500 eV was applied for $LiMg_2H_5$ and $NaMg_2H_5$, and 550 eV for KMg_2H_5 to ensure total-energy convergence. The Brillouin zone was sampled using Monkhorst–Pack k-point meshes [31] of 16 × 6 × 9 for $LiMg_2H_5$ and $NaMg_2H_5$, and 12 × 4 × 13 for KMg_2H_5. The energy convergence tolerance for self-consistent field iterations was set to 5×10^{-6} eV, and the maximum residual stress during structural optimization was constrained below 0.02 GPa. The self-consistent field (SCF) loop convergence criterion was fixed at 5×10^{-7} eV/atom, while the maximum ionic displacement allowed between successive steps was 5×10^{-4} Å. After full relaxation, the equilibrium structures were visualized and analyzed using the VESTA software package [32], which was employed to generate the crystal structure illustrations and to examine atomic

coordination and bonding geometry.

These convergence parameters ensured reliable determination of total energies, atomic forces, and stress tensors, providing high accuracy for the evaluation of structural, electronic, and elastic properties.

Elastic constants (C_{ij}) were calculated using the finite strain method (stress-strain relationship) provided in the CASTEP elasticity tool. For all systems, spin polarization was not included as the compounds are non-magnetic, and DFT + U was not applied since the materials do not contain highly localized d or f electrons. Phonon dispersion relations were derived using the finite displacement method to verify dynamical stability. The use of the GGA-PBE functional without the DFT + U correction was justified by the absence of partially filled d or f orbitals in the constituent Li, Na, K, and Mg atoms, as PBE is known to accurately describe the delocalized s and p states in these systems. Numerical convergence was strictly verified by testing the sensitivity of total energy and stress tensors against the plane-wave cutoff and k-mesh density.

It is important to acknowledge certain methodological limitations inherent in the current DFT approach. First, the GGA-PBE functional is employed for exchange-correlation effects, which is known to systematically underestimate electronic band gaps compared to experimental values. While PBE provides a reliable description of structural and elastic trends, it may also lead to slight deviations in the absolute values of formation energies. Second, vibrational contributions and zero-point energy (ZPE) effects are neglected in the total energy calculations. In hydride systems, H-related vibrational modes can significantly influence thermodynamic stability and desorption enthalpies. Finally, while the present results provide a robust framework for comparing the XMg_2H_5 series, higher-level methods such as GW corrections or hybrid functionals would be required for more precise quantitative alignment with experimental electronic and thermodynamic data.

3. Results and discussions

3.1. Structural properties

The structure of XMg_2H_5 (X = Li, Na, K) is seen in Fig. 1. This quaternary phase crystallizes in the orthorhombic structure with space group Pmmn (No:59). The unit cell of XMg_2H_5 compounds comprises 16 atoms: 2 X atoms (Li, Na, or K), 4 Mg atoms, and 10 H atoms. In the compound $LiMg_2H_5$, the positions of the atoms are as follows: Li occupies the 2a position (0.00000 0.00000 0.61614), Mg is located at the 4e position (0.00000 0.20767 0.25001), and H1 is situated at the 2a position (0.00000, 0.00000, 0.22653), H2 is located at the 4e position (0.00000, 0.18499, 0.86375), H3 is situated at the 4e position (0.00000, 0.36236, 0.49407). In the compound $NaMg_2H_5$, the positions of the Na, Mg, and H atoms are as follows: Na occupies the 2a position at (0.0000, 0.0000, 0.76249), Mg is located at the 4e position (0.0000, 0.18657, 0.28863), and H1 is situated at the 2a position (0.00000, 0.00000, 0.16595), H2 is located at the 4e position (0.00000, 0.22811, 0.84442), H3 is situated at the 4e position (0.00000, 0.36138, 0.48475). In the compound KMg_2H_5, the positions of the K, Mg, and H atoms are as follows: K occupies the 2a position at (0.00000, 0.00000, 0.02636), Mg is located at the 4e position (0.0000, 0.33901, 0.46919), H1 is situated at the 4e position (0.00000, 0.17622, 0.51063), H2 is located at the 4e position (0.00000, 0.35094, 0.97438), H3 is situated at the 2b position (0.00000, 0.50000, 0.47521). All structures were optimized under conditions of zero temperature and pressure. The optimized orthorhombic *Pmmn* structures of $LiMg_2H_5$, $NaMg_2H_5$, and KMg_2H_5 are shown in Fig. 1. The results are presented in Table 1, which includes lattice parameter, unit cell volume, formation energy, and cohesive energy.

To evaluate the thermodynamic stability of XMg_2H_5 (X = Li, Na, K), we performed measurements to ascertain their energy of formation (ΔE_f). The formation energy was determined using the equation presented in Equation (1) [7].

$$\Delta E_f = E_{tot}(XMg_2H_5) - E_{tot}(X) - 2E_{tot}(Mg) - \frac{5}{2}E_{tot}(H_2) \quad (1)$$

In Equation (1), The term $E_{tot}(XMg_2H_5)$ denotes the total energy of the XMg_2H_5 compound. $E_{tot}(X)$, $E_{tot}(Mg)$, and $E_{tot}(H_2)$ denote the total energies of X (Li, Na, K), Mg, and H_2, respectively. The formation energies calculated for $LiMg_2H_5$, $NaMg_2H_5$, and KMg_2H_5 are −0.207 eV, −0.183 eV, and −0.242 eV, respectively. A negative formation energy value signifies thermodynamic stability and the feasibility of experimental synthesis. The findings indicate the thermodynamic stability of all examined materials.

The cohesive energy, represented as E_{coh}, serves as a critical parameter for evaluating system stability. Bond strength denotes the energy necessary to disrupt atomic bonds in a crystal and isolate its individual components. The magnitude of E_{coh} indicates the stability of the crystal. Equation (2) delineates the formula for the cohesive energy of the XMg_2H_5 (X = Li, Na, K) compound [7].

$$E_{coh} = -\frac{1}{10}\left[E_{tot}(XMg_2H_5) - E_{tot}(X) - 2E_{tot}(Mg) - \frac{5}{2}E_{tot}(H_2)\right] \quad (2)$$

The term $E_{tot}(XMg_2H_5)$ denotes the total energy of the XMg_2H_5 compound, while $E_{tot}(X)$, $E_{tot}(Mg)$, and $E_{tot}(H_2)$ represent the energy of each individual atom within the unit cell.

3.2. Elastic properties

Elastic constants play a crucial role in evaluating the mechanical

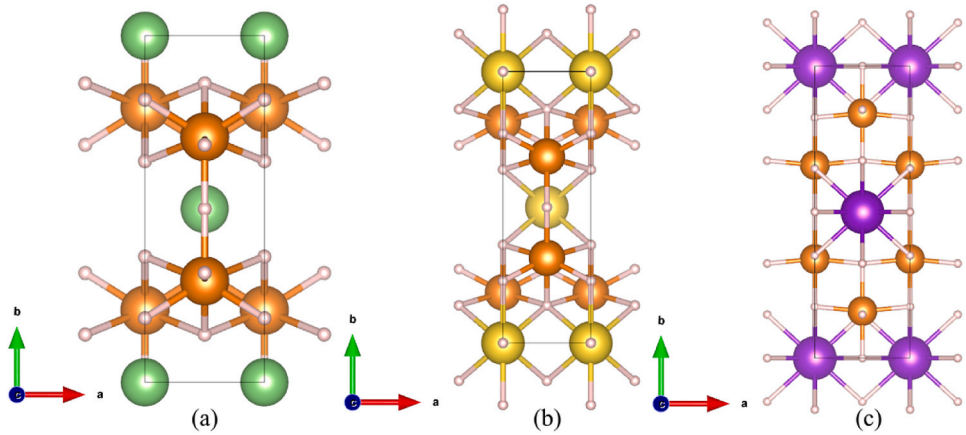

Fig. 1. Optimized crystal structures of (a) $LiMg_2H_5$, (b) $NaMg_2H_5$, and (c) KMg_2H_5. The large spheres represent alkali metal atoms (Li: green, Na: yellow, K: purple), medium-sized spheres indicate Mg atoms (orange), and small spheres correspond to H atoms (pink).

Table 1
Lattice parameters (*a*, *b*, *c*), unit-cell volume (*V*), formation energy (ΔE_f, eV/f.u.), and cohesive energy (E_{coh}, eV/atom) for XMg_2H_5 (X = Li, Na, K).

Material	*a*	*b*	*c*	*V*	ΔE_f	E_{coh}	References
$LiMg_2H_5$	3.1016	8.9930	5.7796	161.21	−0.207	2.924	This study
$NaMg_2H_5$	3.0693	9.4769	6.1932	180.14	−0.183	2.864	This study
KMg_2H_5	4.0773	12.4896	3.8623	196.69	−0.242	2.858	This study

stability, and structural robustness of crystalline materials under external stresses. In the present study, the elastic constants (C_{ij}) of orthorhombic $LiMg_2H_5$, $NaMg_2H_5$, and KMg_2H_5 were calculated using the DFT framework. These constants quantify the material's resistance to deformation and provide direct insight into interatomic bonding strength. Hydrogen storage materials experience repeated expansion and contraction during hydrogen absorption/desorption, resulting in internal stresses that can lead to micro-cracking or pulverization. Therefore, elastic behavior is directly related to the durability and cyclability of the material. High bulk modulus (B) values imply good resistance to volume change, while high shear modulus (G) indicates resistance to shape distortion-both are desirable for reversible hydrogen storage. Conversely, brittleness may cause particle fragmentation upon cycling.

For orthorhombic structures like XMg_2H_5 (X = Li, Na, and K), the mechanical behavior is defined by three separate elastic constants: C_{11}, C_{22}, C_{33}, C_{44}, C_{55}, C_{66}, C_{12}, C_{13}, and C_{23} [33]. These constants show how the crystal responds to stress along different axes. To ensure the mechanical stability of these structures, it is essential to validate adherence to the Born-Huang criteria, which delineate the thermodynamic stability limits for orthorhombic systems through specific inequalities related to these elastic constants.

$$C_{11} + C_{33} - 2C_{13} > 0,\ C_{22} + C_{33} - 2C_{23} > 0,\ C_{11} + C_{22} - 2C_{12} > 0,\ C_{11} > 0,\ C_{22} > 0,\ C_{33} > 0,\ C_{44} > 0,\ C_{55} > 0,\ C_{66} > 0,\ C_{11} + C_{22} + C_{33} + 2(C_{12} + C_{13} + C_{23}) > 0,\ 1/3\ (C_{12} + C_{13} + C_{23}) < B < (C_{11} + C_{22} + C_{33}) \quad (3)$$

Table 2 shows the elastic constants of the orthorhombic structures that were calculated. The data shows that the predicted elastic constants are positive and fit well with the well-known Born stability criterion for an orthorhombic structure, which is provided in equation (3). Therefore, XMg_2H_5 is mechanically stable in this orthorhombic structure.

To evaluate the mechanical stability, stiffness, and ductility of the studied materials, several elastic moduli derived from the elastic constants were analyzed in detail. In this context, the bulk modulus (B), shear modulus (G), Young's modulus (E), Poisson's ratio (υ), and the B/G ratio were calculated to assess the elastic behavior of the compounds. Furthermore, the anisotropy factor (A) was examined to determine the degree of deviation of the crystal structure from isotropic behavior. The calculated elastic parameters are presented in Table 3. The bulk modulus (B) represents a material's resistance to uniform (isotropic) compression, where higher B values indicate lower compressibility and, consequently, a more rigid structure. The shear modulus (G) reflects the resistance of atomic bonds to shear deformation. According to the calculated results, the $LiMg_2H_5$ compound exhibits the highest stiffness with B = 45.27 GPa and G = 35.22 GPa, while $NaMg_2H_5$ shows the lowest elastic strength with B = 22.48 GPa and G = 19.53 GPa. These findings suggest that the presence of lithium enhances the ionic bonding strength, leading to a denser atomic arrangement and a more compact crystal structure. The Young's modulus (E) characterizes the stiffness of a material under elastic deformation and indicates its resistance to externally applied stresses. The calculated results reveal that $LiMg_2H_5$ exhibits the highest rigidity with E = 83.91 GPa, followed by KMg_2H_5 (E = 64.39 GPa) and $NaMg_2H_5$ (E = 48.64 GPa). These findings indicate that the Li-containing compound is structurally more rigid and less susceptible to elastic deformation compared to the other two hydrides. Poisson's ratio (υ) defines the lateral expansion tendency of a material when subjected to longitudinal stress. Typically, materials with $\upsilon < 0.26$ are considered brittle, whereas those with $\upsilon > 0.26$ exhibit ductile characteristics. According to the results, all compounds have Poisson's ratios in the range of 0.19–0.24, confirming their brittle nature. This observation is consistent with the general mechanical behavior of metal hydrides, which are known for their intrinsic brittleness. Another important criterion for evaluating ductility is the Pugh ratio (B/G). Materials with B/G > 1.75 are classified as ductile, while those with B/G < 1.75 are brittle. The obtained values (1.29 for $LiMg_2H_5$, 1.63 for $NaMg_2H_5$, and 1.37 for KMg_2H_5) indicate that all three compounds are brittle, although $NaMg_2H_5$ exhibits relatively higher ductility among them due to its higher B/G ratio. The machinability index (μ^M) was evaluated as B/C_{44} in the study, and it was accepted that higher μ^M values indicate better machinability. In this context, KMg_2H_5 (μ^M = 2.36) exhibits the best machinability, while $NaMg_2H_5$ (μ^M = 1.56) shows moderate machinability and $LiMg_2H_5$ (μ^M = 1.07) shows the lowest machinability.

Table 2
Calculated elastic constants (C_{ij}, GPa) and derived parameters (C′, C_p, ζ) for orthorhombic $LiMg_2H_5$, $NaMg_2H_5$, and KMg_2H_5 hydrides.

Parameters	$LiMg_2H_5$	$NaMg_2H_5$	KMg_2H_5
C_{11}	98.66	88.99	68.81
C_{22}	111.33	97.77	61.27
C_{33}	66.50	37.63	86.81
C_{44}	42.43	20.39	15.50
C_{55}	36.51	23.50	31.80
C_{66}	32.46	7.91	41.83
C_{12}	15.69	12.00	26.18
C_{13}	24.46	14.43	15.49
C_{23}	28.28	16.13	15.22
C'	41.48	38.49	21.31
C_p	−12.05	−9.08	−5.38
ζ	0.31	0.29	0.52

According to the data presented in Table 4, the $NaMg_2H_5$ compound exhibits the highest values of the universal anisotropy index (A^U = 1.9568) and related sub-metrics (A_B, A_G, d_E, A^{eq}, and A^L), indicating a strong dependence of its elastic behavior on the crystallographic orientation. In contrast, $LiMg_2H_5$ demonstrates the lowest anisotropy parameters, reflecting an almost isotropic elastic nature. The KMg_2H_5 compound occupies an intermediate position, showing a moderate level of anisotropy between the two extremes. Overall, $NaMg_2H_5$ exhibits the most direction-dependent elastic response, whereas $LiMg_2H_5$ behaves more homogeneously. These results clearly indicate that the substitution of alkali metals (Li → Na → K) significantly influences the anisotropic characteristics of the hydrides and enhances the directional variation in their mechanical responses.

In storage environments, elastic anisotropy ($A \neq 1$) affects processing and operation by inducing direction-dependent deformation during powder compaction and pelletization, leading to non-uniform stress distribution. During hydrogen absorption/desorption cycles, anisotropic lattice strain can promote localized stress accumulation and microcrack formation, potentially reducing mechanical durability. Therefore, lower elastic anisotropy is advantageous for maintaining structural integrity and reliable operation under repeated hydrogen storage cycles.

The elastic properties of XMg_2H_5 (X = Li, Na, K) serve as a fundamental indicator of their structural response during the repetitive lattice expansion and contraction inherent in hydrogen absorption/desorption cycling. During hydrogenation, the interstitial occupation of hydrogen induces significant internal strain; materials with a high bulk modulus (B), such as $LiMg_2H_5$ (45.27 GPa), demonstrate a superior ability to accommodate these stresses without undergoing immediate lattice

Table 3
Polycrystalline elastic moduli derived from C(ij): Voigt/Reuss/Hill bulk (B_V, B_R, B_H), shear (G_V, GR, G_H), Young's modulus *E*, Pugh ratio B/G, Poisson's ratio *ν*, and machinability index μ^M for XMg_2H_5.

Compound	B_V	B_R	B_H	G_V	G_R	G_H	E	B/G	υ	μ^M
$LiMg_2H_5$	45.93	44.62	45.27	36.15	34.30	35.22	83.91	1.29	0.19	1.07
$NaMg_2H_5$	34.39	29.23	22.48	22.48	16.58	19.53	48.64	1.63	0.24	1.56
KMg_2H_5	36.74	36.51	36.63	28.49	24.85	26.67	64.39	1.37	0.21	2.36

Table 4
Calculated elastic anisotropy parameters of orthorhombic XMg_2H_5 (X = Li, Na, K) hydrides, including shear anisotropy factors (*A*, A_1, A_2, A_3), bulk and shear anisotropy indices (A_B, A_G), universal anisotropy index (A^U), directional Young's modulus difference (d_E), equivalent anisotropy factor (A^{eq}), and elastic limit anisotropy (A^L).

Parameters	$LiMg_2H_5$	$NaMg_2H_5$	KMg_2H_5
A	1.0228	0.5296	0.7274
A_1	1.4599	0.8341	0.4975
A_2	1.2041	0.9115	1.0811
A_3	0.6008	0.5133	1.6162
A_B	0.0145	0.0812	0.0031
A_G	0.0263	0.1511	0.0683
A^U	0.2995	1.9568	0.7390
d_E	2.5099	2.8208	2.5960
A^{eq}	1.6397	1.9568	2.1509
A^L	0.0290	0.1617	0.0062

distortion or mechanical failure. Conversely, the degree of elastic anisotropy (A^U) is directly linked to the development of micro-cracks at grain boundaries. In highly anisotropic systems like $NaMg_2H_5$ (A^U = 1.9568), the non-uniform directional expansion creates localized stress concentrations, which act as precursors for mechanical degradation and particle pulverization over extended cycling. Furthermore, the G/B ratio (Pugh's ratio) and Poisson's ratio indicate that the inherent brittleness of these hydrides necessitates a robust elastic framework to maintain structural integrity. By quantifying these elastic parameters, we can predict the 'mechanical fatigue' resistance of the host lattice, which is a decisive factor in determining the long-term cycle life and safety of solid-state hydrogen storage systems.

As presented in Table 5, the calculated Vickers hardness values reveal the comparative resistance of the studied compounds to plastic deformation. The highest average hardness is observed for $LiMg_2H_5$ (HV_{avg} = 6.98 GPa), indicating strong ionic bonding and a compact crystal lattice. In contrast, $NaMg_2H_5$ exhibits the lowest hardness (HV_{avg} = 3.26 GPa), which can be attributed to weaker interatomic bonding and a relatively loose atomic arrangement. The KMg_2H_5 compound displays a moderate hardness of HV_{avg} = 5.09 GPa, representing a transitional mechanical behavior between the Li- and Na-based hydrides. The observed hardness trend ($LiMg_2H_5$ > KMg_2H_5 > $NaMg_2H_5$) is in good agreement with the corresponding elastic moduli (E and G), confirming that higher elastic stiffness directly correlates with greater hardness. Overall, the results demonstrate that the hardness of metal hydrides strongly depends on the strength of ionic bonding, the degree of atomic packing, and bond topology within the crystal structure.

The assessment of Vickers hardness (H_V) and the machinability index (μ^M) provides essential insights into the structural durability and practical handling of powdered XMg_2H_5 (X = Li, Na, K) hydrides. Although these materials are typically utilized in powdered form, they are often processed into pellets or compact blocks to optimize volumetric density and thermal management within storage tanks. In this context, Vickers hardness is a critical parameter for evaluating the resistance of these hydrides to plastic deformation during the compaction process and for predicting their structural stability under the internal stresses generated by repeated hydrogen absorption and desorption cycles. Furthermore, the machinability index reflects the material's response to mechanical strain; a higher index, as observed in KMg_2H_5 (μ^M = 2.36), suggests better adaptability during the fabrication of hydride-based reactors. These mechanical indicators also serve as proxies for 'pulverization resistance,' where higher hardness levels, particularly in $LiMg_2H_5$ (H_V = 6.98 GPa), indicate a greater ability to maintain particle morphology and prevent excessive fragmentation (pulverization) during long-term operational cycling. Therefore, integrating these mechanical metrics is vital for designing robust solid-state storage systems that can withstand mechanical degradation over thousands of cycles.

As presented in Table 6, the volumetric elastic parameters indicate that $LiMg_2H_5$ exhibits the highest rigidity with an average bulk modulus of B_{relax} = 44.62 GPa, while $NaMg_2H_5$ possesses the lowest value (B_{relax} = 29.23 GPa), and KMg_2H_5 occupies an intermediate position (B_{relax} = 36.51 GPa). The comparison of directional bulk moduli (B_a, B_b, B_c) reveals significant differences among the crystallographic axes in $NaMg_2H_5$, which is consistent with its large anisotropy ratios (α = 0.84, β = 3.06). In contrast, $LiMg_2H_5$ displays smaller anisotropy parameters (α = 0.81, β = 1.52), suggesting a nearly isotropic elastic behavior, whereas KMg_2H_5 shows moderate and balanced directional responses (α = 1.22, β = 0.94). These findings clearly demonstrate that the type of alkali metal atom (Li, Na, K) strongly influences both the compressibility and the elastic anisotropy of the hydrides. Specifically, the incorporation of Na increases directional asymmetry in bonding, leading to the highest degree of anisotropy, while $LiMg_2H_5$ exhibits the most homogeneous and isotropic elastic response.

The directional elastic metrics summarized in Table 7 indicate that the $NaMg_2H_5$ compound exhibits the highest anisotropy in E, B, and G moduli (A_E = 0.28, A_B = 0.44, A_G = 0.25). In contrast, $LiMg_2H_5$ presents lower anisotropy indices, reflecting a more homogeneous elastic response, while KMg_2H_5 demonstrates an almost isotropic volumetric behavior with A_B = 0.07. Notably, the presence of B_{min} < 0 (−2.33 TPa^{-1}) in $NaMg_2H_5$ suggests the possibility of negative linear

Table 6
Volumetric elastic parameters: relaxed bulk modulus B_{relax} and directional components (B_a, B_b, B_c), with anisotropy indicators α and β.

Compound	B_{relax}	B_a	B_b	B_c	α	β
$LiMg_2H_5$	44.62	148.58	184.19	97.52	0.81	1.52
$NaMg_2H_5$	29.23	143.23	171.18	46.75	0.84	3.06
KMg_2H_5	36.51	115.30	94.35	123.25	1.22	0.94

Table 5
Calculated Vickers hardness values (H_V, GPa) of orthorhombic $LiMg_2H_5$, $NaMg_2H_5$, and KMg_2H_5 hydrides estimated using different theoretical models (Chen, Tian, Teter, Miao, and Mazhnik) along with their average hardness $(H_V)_{avg}$.

Compound	$(H_V)_{Chen}$	$(H_V)_{Tian}$	$(H_V)_{Teter}$	$(H_V)_{Miao}$	$(H_V)_{Mazhnik}$	$(H_V)_{avg}$
$LiMg_2H_5$	8.98	8.61	5.32	7.25	4.74	6.98
$NaMg_2H_5$	3.34	4.33	2.95	3.32	2.24	3.26
KMg_2H_5	6.42	6.56	4.03	5.21	3.26	5.09

Table 7
Directional elastic parameters and hardness anisotropy indices of orthorhombic XMg_2H_5 (X = Li, Na, K) hydrides. The table presents the maximum and minimum values of Young's modulus (E_{max}/E_{min}), bulk modulus (B_{max}/B_{min}), shear modulus (G_{max}/G_{min}), and Vickers hardness (H_{vmax}/H_{vmin}), along with their respective anisotropy indices (A_E, A_B, A_G, A_{Hv}).

Compound	E_{max}	E_{min}	A_E	B_{max}	B_{min}	A_B	G_{max}	G_{min}	A_G	H_{vmax}	H_{vmin}	A_{H_v}
$LiMg_2H_5$	103.55	54.98	0.18	61.39	32.51	0.19	44.48	25.74	0.12	21.47	4.27	0.41
$NaMg_2H_5$	90.42	27.04	0.28	57.05	15.58	0.44	40.60	7.91	0.25	17.51	−2.33	inf
KMg_2H_5	84.85	42.42	0.17	41.08	31.45	0.07	41.82	15.50	0.21	21.79	0.17	0.59

compressibility along certain crystallographic directions, leading to an $A_{\beta 1} = \infty$ result. This phenomenon implies that under hydrostatic loading, direction-dependent deformation becomes pronounced, and the crystallographic texture should be carefully considered in mechanical design. Overall, the introduction of Na into the hydride lattice induces bond-directional asymmetry, resulting in the most anisotropic elastic response among the compounds studied.

Generally, a value of "0" in anisotropy indices indicates perfect

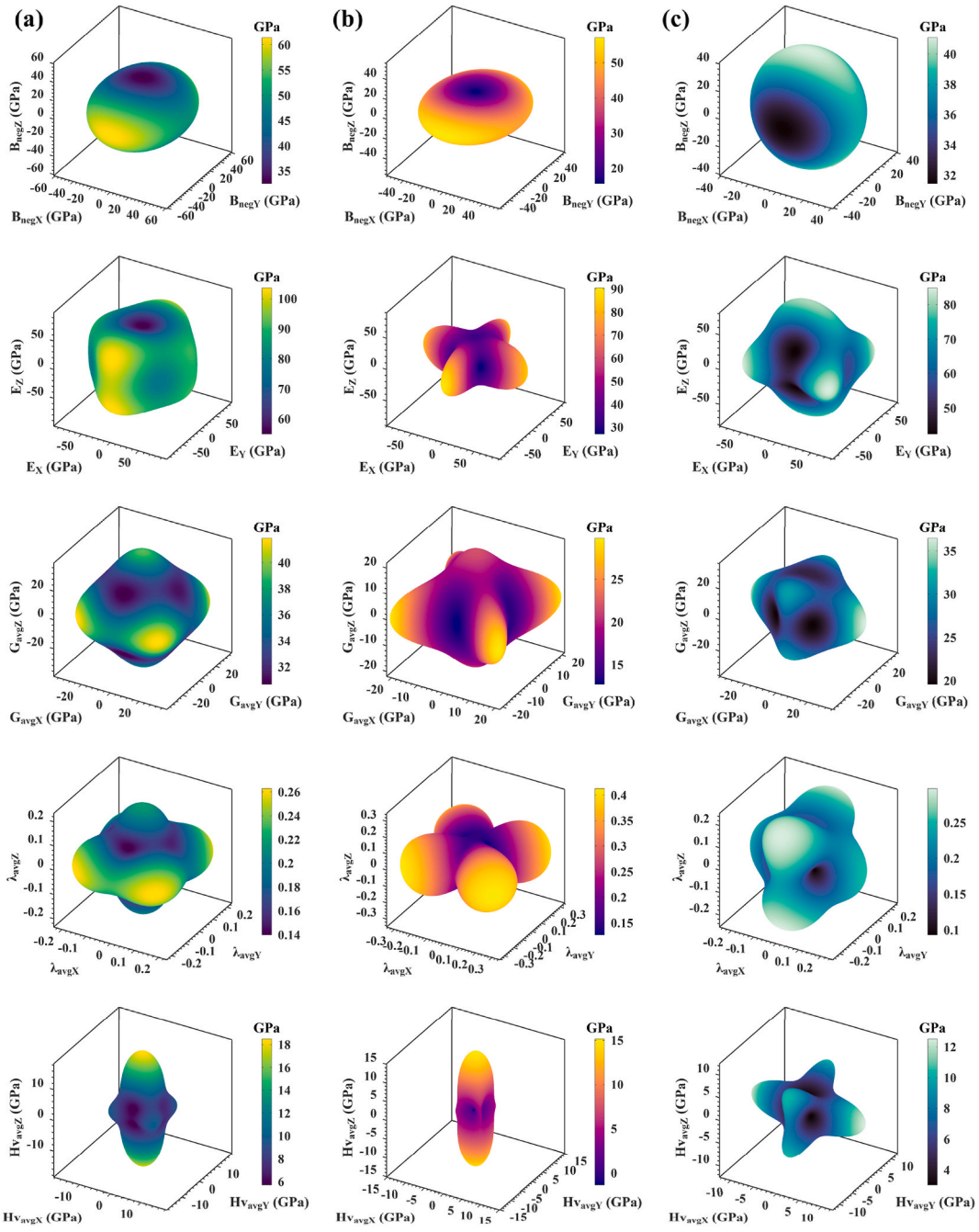

Fig. 2. Three-dimensional anisotropy surfaces of orthorhombic XMg_2H_5 (X = Li, Na, K) hydrides: (a) $LiMg_2H_5$, (b) $NaMg_2H_5$, and (c) KMg_2H_5. The directional distributions of bulk modulus (B), Young's modulus (E), shear modulus (G), Poisson's ratio (ν), and Vickers hardness (H_V) are illustrated.

isotropy (same properties in all directions). An increase in the value in either the negative or positive direction indicates an increase in the material's directional dependence. The negative value of the hardness anisotropy index for $NaMg_2H_5$ (−2.33) highlights the significant disparity in mechanical resistance along different crystallographic directions. This pronounced negative value is a direct consequence of the weaker atomic bonding in specific planes compared to $LiMg_2H_5$, making $NaMg_2H_5$ the most anisotropic compound in the studied series.

The three-dimensional (3D) anisotropy surfaces of $LiMg_2H_5$, $NaMg_2H_5$, and KMg_2H_5 are presented in Fig. 2(a–c). The directional distributions of the bulk modulus, Young's modulus, shear modulus, Poisson's ratio, and Vickers hardness reveal distinct elastic and mechanical anisotropies among the compounds. $LiMg_2H_5$ exhibits nearly spherical surfaces, implying a more isotropic and mechanically stable character, while $NaMg_2H_5$ shows highly distorted and elongated shapes, indicating pronounced anisotropy and directional dependence of stiffness and hardness. KMg_2H_5 lies between these two extremes, displaying moderate anisotropy. These results confirm that alkali-metal substitution significantly influences the elastic and hardness anisotropy of XMg_2H_5 hydrides, with Li-substituted compounds being the most isotropic and mechanically robust.

The systematic variations in the physical properties of the XMg_2H_5 series are illustrated in Fig. 3, providing a clear visualization of the trends driven by alkali metal substitution. As shown in Fig. 3(a–b), the lattice parameters and unit-cell volume exhibit a consistent expansion as the ionic radius increases from Li^+ to K^+. This structural dilation directly correlates with the observed mechanical softening; specifically, the elastic moduli (B, G, E) reach their maximum in the compact $LiMg_2H_5$ lattice and show a significant reduction in the expanded $NaMg_2H_5$ system (Fig. 3(d)). Furthermore, the formation energy remains negative across the entire series (Fig. 3(c)), confirming that thermodynamic stability is maintained despite the substantial changes in structural volume and mechanical stiffness.

3.3. Electronic properties

The electronic band structure and the corresponding total and projected density of states (PDOS) of the Li–Mg–H compound is presented in Fig. 4(a). As seen from the band dispersion along the high-symmetry directions in the Brillouin zone, the material exhibits a direct band gap of 2.97 eV at the Γ-point. The relatively large band gap confirms the semiconducting nature of the compound, suggesting its potential for optoelectronic and hydrogen-storage-related applications where electronic insulation is favorable. The PDOS analysis reveals that the H-s states play a dominant role in the formation of both the valence band maximum (VBM) and conduction band minimum (CBM). This finding highlights the crucial role of hydrogen in defining the electronic character of the compound, consistent with the expected ionic bonding nature of complex hydrides. In contrast, the Li-s and Mg-s states contribute only marginally near the band edges, indicating that alkali and alkaline-earth atoms primarily act as charge donors, stabilizing the lattice but contributing less to the band-edge electronic states.

The band structure and PDOS of the Na–Mg–H compound is illustrated in Fig. 4(b). The calculated band gap is 3.07 eV, which is larger than that of many conventional hydrides, indicating that the material belongs to the class of wide band gap semiconductors. Unlike direct-gap semiconductors, the Na–Mg–H compound exhibits an indirect band gap, since the valence band maximum (VBM) and conduction band minimum (CBM) are located at different high-symmetry points of the Brillouin zone. This indirect nature is expected to result in weaker optical

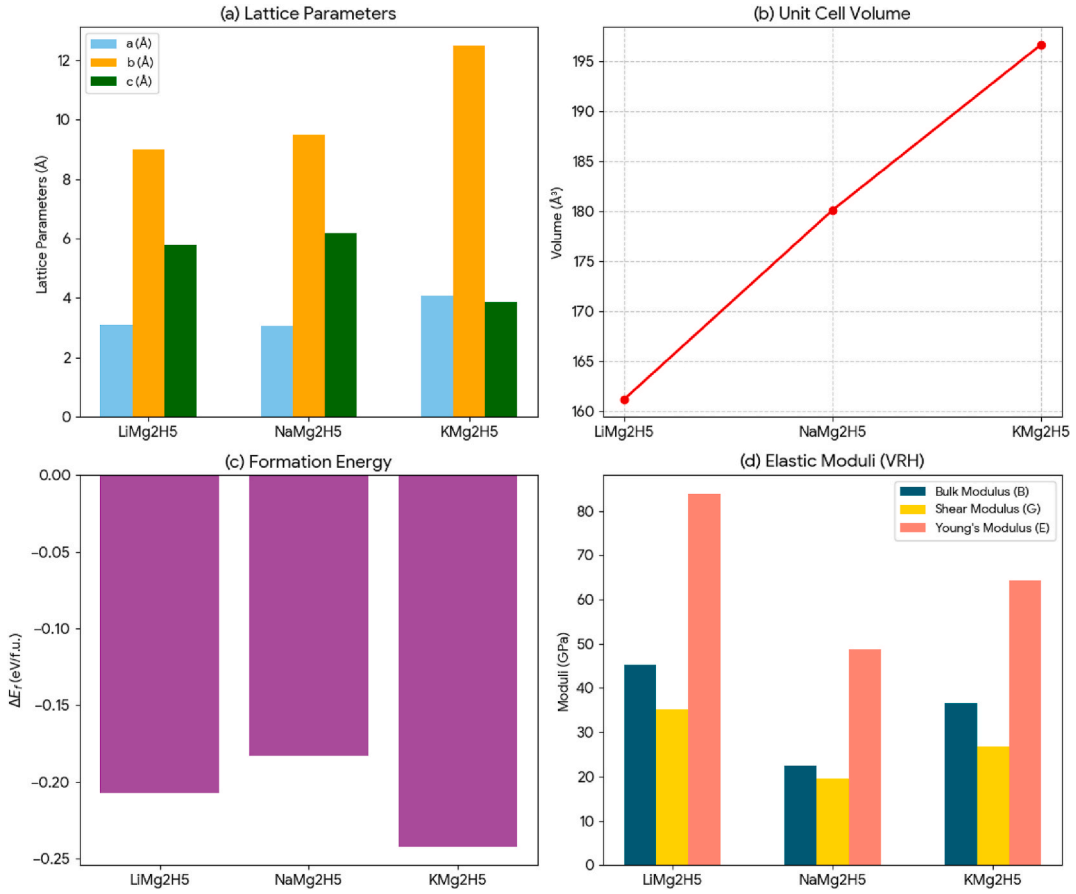

Fig. 3. Consolidated trends of physical properties for XMg_2H_5 (X = Li, Na, K) series: (a) Lattice parameters (a, b, c), (b) unit-cell volume, (c) formation energy (ΔE_f), and (d) VRH-averaged elastic moduli (Bulk, Shear, and Young's moduli).

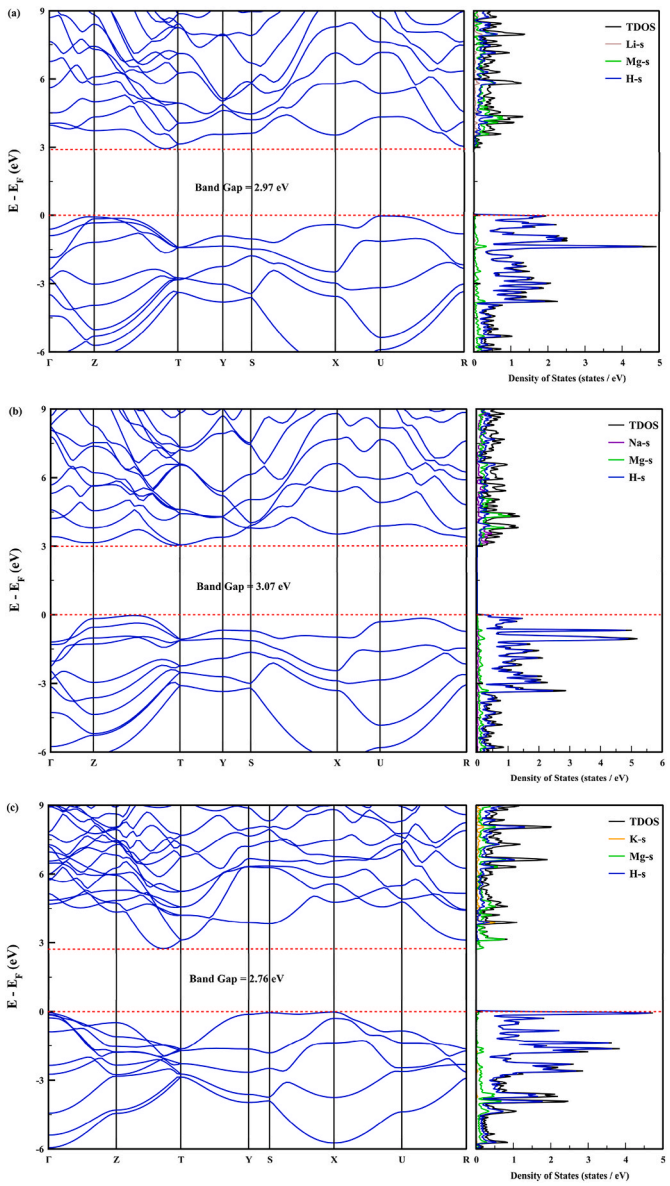

Fig. 4. Electronic band structure and density of states for (a) $LiMg_2H_5$, (b) $NaMg_2H_5$, and (c) KMg_2H_5.

absorption efficiency, which may limit its optoelectronic performance. However, the presence of a sizable band gap is still advantageous for hydrogen storage applications, as suppressed electronic conductivity reduces energy losses during reversible storage processes.

The PDOS analysis further clarifies the orbital contributions to the electronic structure. The valence band near the Fermi level is dominated by H–s orbitals, with additional but smaller contributions from Mg–s states. On the other hand, the conduction band minimum primarily originates from Na–s and Mg–s orbitals, suggesting that hydrogen states largely govern the occupied bands, while metal states stabilize the unoccupied ones. This distribution highlights the crucial role of hydrogen in determining the electronic behavior of the compound, while Na and Mg mainly act as electron donors supporting the hydride framework. In addition, the conduction bands of the Na–Mg–H system are relatively dispersive, which implies lower effective masses for electrons and potentially higher carrier mobility compared to other alkali-based hydrides. This feature could positively influence charge transport and diffusion-related processes within the lattice, although the indirect band gap character might still restrict strong optical transitions. Overall, the electronic structure analysis confirms that Na–Mg–H is a wide-gap, semiconducting hydride, in which hydrogen plays a central role in defining its electronic characteristics, making it a promising material for hydrogen storage applications. The band structure and PDOS of the K–Mg–H compound is illustrated in Fig. 4(c). The calculated band gap is 2.76 eV, which is slightly smaller than that of the Li–Mg–H compound. In contrast to the direct gap nature of the Li-based system, the K–Mg–H compound exhibits an indirect band gap, as the valence band maximum and conduction band minimum are located at different high-symmetry points. This indirect gap character generally leads to weaker optical absorption efficiency compared to direct-gap semiconductors, which may influence its optoelectronic performance. Nevertheless, its semiconducting nature remains significant for practical applications in hydrogen storage systems where electronic conductivity suppression is beneficial. The PDOS analysis again confirms that H-s orbitals dominate near the Fermi level, particularly around the VBM and CBM, emphasizing the central role of hydrogen in determining the electronic properties of the hydride. The contribution from K-s and Mg-s states is limited, supporting the view that alkali and alkaline-earth metals mainly donate electrons to stabilize the hydride framework. Interestingly, the conduction band structure of the K-based compound is slightly flatter compared to the Li counterpart, implying heavier effective masses for electrons and consequently lower carrier mobility. This distinction may have implications for diffusion-related electronic processes within the lattice.

The semiconducting nature of XMg_2H_5 compounds is beneficial for hydrogen storage for several reasons. Firstly, a well-defined band gap indicates a high degree of ionic–covalent bonding stability within the hydride framework, which is essential for structural integrity during cycling. Secondly, the suppression of electronic conductivity—characteristic of wide-bandgap semiconductors—tends to reduce parasitic charge-driven hydrogen loss and energy dissipation during reversible storage processes. This electronic insulation is favorable for maintaining the stability of the hydride at room temperature while allowing for controlled hydrogen release upon thermal activation.

3.4. Optical properties

Optical properties derived from first-principles density functional theory (DFT) calculations provide direct insight into the electronic excitations, interband transition channels, screening behaviour, and collective electronic responses of a material. In practice, the frequency-dependent complex dielectric function, $\varepsilon(\omega) = \varepsilon_1(\omega) + i\varepsilon_2(\omega)$, is computed from the calculated Kohn–Sham states (within the independent-particle approximation or with additional many-body corrections) and is then used to derive a set of experimentally measurable optical constants such as the absorption coefficient, refractive index, reflectivity, optical conductivity and energy-loss function. These optical fingerprints report on transition energies (linked to the band structure and band gap), the orbital character of participating states, and the degree of electronic screening and plasmonic response. For hydride materials and hydrogen storage applications, optical properties are relevant for several reasons. First, the onset of optical absorption and the strength of interband transitions provide an alternative probe of the band gap and the direct/indirect nature of electronic transitions - information that affects photogenerated carriers and any photo-assisted hydrogen release processes. Second, the static and low-frequency dielectric response quantify electronic screening and polarizability; higher screening can modify hydrogen binding energies and diffusion barriers through changes in Coulomb interactions. Third, optical conductivity and loss spectra (plasmon peaks) reflect free-carrier and collective responses that change upon hydrogenation/dehydrogenation and thus can be used as non-destructive spectroscopic diagnostics. Finally, the wavelength range over which the material is transparent, or absorbing determines how optical or spectroscopic techniques (UV–Vis, EELS, IR) can be applied to monitor hydrogen uptake and structural

changes in operando. Consequently, a detailed panel-by-panel analysis of the computed optical functions is informative both for fundamental understanding and for practical sensing or device design in hydrogen storage research.

Fig. 5(a–c) show the real and imaginary parts of the dielectric function for LiMg2H5, $NaMg_2H_5$, and KMg_2H_5, respectively.

The real part $\varepsilon_1(\omega)$ and imaginary part $\varepsilon_2(\omega)$ for the Li-based compound show a pronounced absorption band (peak in ε_2) centered at low to mid-ultraviolet energies (roughly in the 4–7 eV window in the plotted curves). The relatively large magnitude of ε_2 at that energy indicates strong interband transitions, consistent with allowed transitions from hydrogen-derived valence states into metal-dominated conduction states. The real part exhibits dispersive behavior: ε_1 decreases with energy across the main absorption and crosses through a region of reduced positive value beyond the peak, consistent with resonant screening associated with those interband excitations. The relatively large low-energy (near-static) ε_1 indicates moderate electronic polarizability. Together, these features imply that the Li compound supports stronger optical transitions and higher polarizability than the heavier alkali analogues, a result that can be traced back to stronger orbital overlap and wider band dispersion in the Li system. The Na analogue shows qualitatively similar structure in $\varepsilon_2(\omega)$ but with slightly reduced peak intensity and a small shift in the main absorption maximum compared to the Li system. The lower ε_2 amplitude indicates somewhat weaker transition matrix elements or reduced joint density of states at those excitation energies. $\varepsilon_1(\omega)$ follows the expected dispersive trend with a moderate static value and a pronounced variation near the absorption band. These observations are consistent with the Na compound having slightly narrower bandwidths and weaker overlap than the Li case, producing less intense optical transitions while still maintaining significant absorptive behaviour in the UV. For the K-based compound the imaginary part ε_2 displays the smallest peak intensity among the three, and the main absorption feature is slightly red-shifted (toward lower energy) relative to Li and Na. The real part shows a comparable, though somewhat reduced, low frequency ε_1. The reduced ε_2 suggests weaker optical transition strength, in line with the K system's larger ionic radius, decreased orbital overlap and heavier effective masses inferred from the band structure. The redshift and weakened intensity of optical transitions in KMg_2H_5 are consistent with more localized states and an increased indirect character of transitions.

Fig. 5(d) shows the refractive index as a function of energy for $LiMg_2H_5$, $NaMg_2H_5$, and KMg_2H_5. The refractive index spectra for the three compounds show a prominent peak in the near-UV (a few eV), followed by a decrease toward higher energies and a gradual rise at the highest energies shown. The static (zero-frequency or low-energy) refractive index is moderate (on the order of ~2 for these compounds), with $LiMg_2H_5$ giving the largest static index and KMg_2H_5 the smallest. This trend mirrors the differences in low-frequency $\varepsilon 1$ and indicates that the Li system is the most optically dense and polarizable at low photon energies. From a hydrogen storage perspective, the static dielectric response (and hence n(0)) influences Coulomb screening and can affect the energetics of charged defects and hydrogen diffusion barriers; materials with larger dielectric screening generally reduce Coulombic interactions and can modify migration energies.

Fig. 5(e–h) show the absorption coefficient, reflectivity, conductivity, and loss function as a function of energy for $LiMg_2H_5$, $NaMg_2H_5$, and KMg_2H_5, respectively. All three spectra show an absorption onset in the near-UV and a broad, intense absorption band extending through the UV (the plotted scale shows a strong peak in the several-eV range). $LiMg_2H_5$ exhibits the largest peak absorption coefficient, $NaMg_2H_5$ is intermediate, and KMg_2H_5 the weakest. The absorption of onset energy is closely connected to the electronic band gap and the allowedness of transitions; the stronger absorption for Li is consistent with a relatively more direct/allowed character and stronger transition matrix elements, whereas the

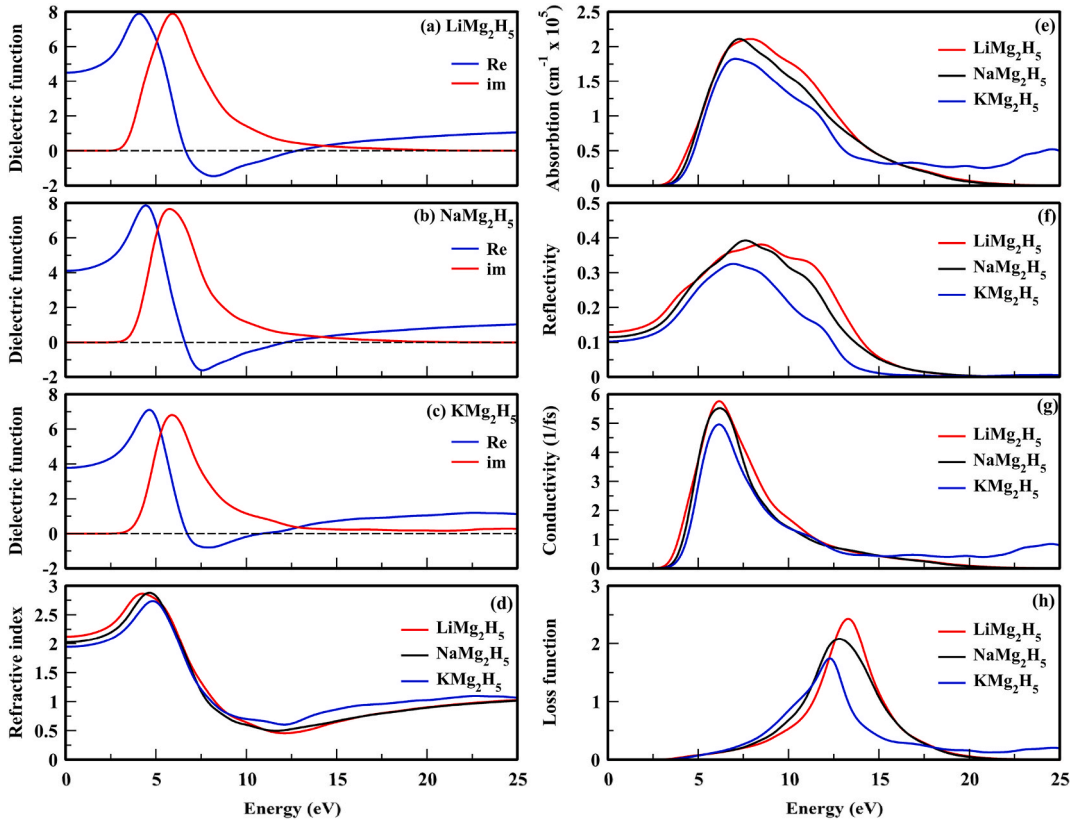

Fig. 5. (a–c) frequency-dependent dielectric function ($\varepsilon_1(\omega)$, $\varepsilon_2(\omega)$), d) Refractive index spectra $n(\omega)$, e) Absorption coefficient $\alpha(\omega)$, f) reflectivity $R(\omega)$, g) optical conductivity $\sigma(\omega)$, and h) energy-loss function (ELF) for $LiMg_2H_5$, $NaMg_2H_5$, and KMg_2H_5.

weaker absorption in K is consistent with more indirect or less allowed transitions. Practically, stronger absorption at lower energies enables optical probing (UV–Vis) of electronic changes upon hydrogenation, while weaker absorption makes optical detection more challenging but may reduce photogenerated carrier effects in applications. Reflectivity spectra show a broad maximum in the UV (roughly in the same energy window as the absorption peaks) with magnitudes that follow the order Li > Na > K. Reflectivity at low photon energies is relatively low, suggesting moderate transparency in the visible-near-infrared region for all three hydrides. The UV reflectance maxima correlate with the dielectric response and are symptomatic of strong interband transitions and increased refractive index in that spectral window. For device design or spectroscopic monitoring, the low visible reflectivity implies that reflectometric techniques would be more informative in the UV range where the materials exhibit stronger optical contrast. The computed real part of the optical conductivity shows a pronounced peak co-located with the main absorption band; Li shows the largest peak conductivity, Na intermediate and K lowest. Because optical conductivity is proportional to the joint density of states and transition probability, the behaviour mirrors the trends seen in ε_2 and the absorption. The relatively low conductivity at low energies (near DC limit) confirms a semiconducting character with small intrinsic free-carrier contribution — a favorable attribute for reversible hydrogen storage because suppressed electronic conductivity tends to reduce parasitic charge-driven hydrogen loss mechanisms. The relative magnitudes of the optical conductivity peaks also inform on how efficiently photoexcited carriers could be generated and participate in diffusion or reaction processes. The loss function exhibits a distinct plasmon-like peak for each compound in the UV (roughly around 9–12 eV in the plotted curves). $LiMg_2H_5$ shows the highest-energy and most intense plasmon peak, $NaMg_2H_5$ is slightly lower in energy/intensity, and KMg_2H_5 displays the lowest plasmon energy and smallest amplitude. These plasmon positions reflect the effective delocalized electron density and screening in the compounds: a higher plasmon energy signifies a larger free-electron-like response (higher effective valence electron density or stronger itinerancy), while the downward shift for the heavier alkali indicates reduced free-electron character. The plasmonic behavior can be probed directly by electron energy-loss spectroscopy (EELS) and is sensitive to changes in electron density upon hydrogen uptake/release-thus making the loss function a useful diagnostic for hydrogenation state and for understanding collective electronic effects that may influence desorption kinetics. The full set of calculated optical functions paints a consistent picture: substituting the alkali metal from Li → Na → K progressively reduces the intensity of interband optical transitions, slightly red shifts the principal features, and lowers the plasmon energy. These trends are consistent with larger cation size, reduced orbital overlap, narrower band dispersion and heavier effective masses in the heavier alkali systems. From a hydrogen storage viewpoint, the semiconducting character and low low-frequency optical conductivity are advantageous for reversible storage because they minimize electronic leakage and non-thermally driven loss channels; meanwhile, the computed absorption, reflectivity and loss spectrum provide concrete spectral windows (mainly in the UV) where optical and EELS experiments can monitor hydrogenation and electronic-structure changes. Finally, because standard DFT approximations (e.g., GGA/PBE) tend to underestimate fundamental gaps, we recommend that the qualitative spectral trends described here be combined with higher-level many-body corrections (GW, hybrid functionals) if precise quantitative agreement with experiment is required, particularly for absorption edge positions and plasmon energies.

The calculated optical constants, particularly the absorption coefficient and energy-loss spectra, serve as vital diagnostic tools for hydrogen sensing applications. The distinct shift in plasmon peaks (9–12 eV) and changes in reflectivity upon alkali-metal substitution provide unique spectroscopic fingerprints. These characteristics enable the monitoring of hydrogenation/dehydrogenation states in real-time through non-destructive optical techniques such as UV–Vis spectroscopy or Electron Energy-Loss Spectroscopy (EELS). Thus, these results are not only fundamental but also offer a theoretical basis for designing optical-based hydrogen sensors and diagnostics for hydride performance.

3.5. Thermodynamic properties

The thermophysical parameters of the $LiMg_2H_5$, $NaMg_2H_5$, and KMg_2H_5 compounds, including the density (ρ), transverse (v_t), longitudinal (v_l), and average sound velocities (v_m), melting temperature (T_m), Debye temperature (θ_D), minimum thermal conductivity (K_{min}), and Grüneisen parameter (γ), are summarized in Table 8.

These parameters provide crucial insights into the lattice dynamics, thermal stability, and heat transport characteristics of the hydrides. The Debye temperature (θ_D) represents a fundamental physical parameter that significantly influences a material's lattice vibrations, melting behavior, thermal expansion, specific heat capacities, and thermal conductivity. It serves as a key indicator for differentiating between the low- and high-temperature regimes of a solid. The Debye temperature can be calculated using the following relation [34]:

$$\theta_D = \frac{h}{k_B}\left[\left(\frac{3N}{4\pi}\right)\frac{N_A\rho}{M}\right]^{\frac{1}{3}} v_m \tag{4}$$

Here, h, k_B, N, N_A, ρ, M, and v_m denote Planck's constant, Boltzmann's constant, the number of atoms per formula unit, Avogadro's number, density, molar mass, and the average sound velocity, respectively. Furthermore, for isotropic materials, the average sound velocity (v_m) can be determined from the longitudinal (v_l) and transverse (v_t) sound velocities using the following relation [34]:

$$v_m = \left[\frac{1}{3}\left(\frac{2}{v_t^3} + \frac{1}{v_l^3}\right)\right]^{-\frac{1}{3}} \tag{5}$$

The longitudinal (v_l) and transverse (v_t) sound velocities can be expressed in terms of the polycrystalline bulk and shear moduli based on the relations formulated by Voigt and Reuss [35]:

$$v_l = \sqrt{\frac{3B + 4G}{3\rho}} \quad \text{and} \quad v_t = \sqrt{\frac{G}{\rho}} \tag{6}$$

The longitudinal (v_l) and transverse (v_t) sound velocities are directly related to the bulk modulus and the density of the material.

Among the investigated hydrides, $LiMg_2H_5$ exhibits the highest sound velocities (v_t = 5312.19 m/s, v_l = 8596.23 m/s, and v_m = 5859.01 m/s) and the largest Debye temperature (θ_D = 807.62 K). These results indicate a relatively strong interatomic bonding and high lattice stiffness, implying that $LiMg_2H_5$ possesses the most rigid lattice structure among the studied compounds.

The melting temperature (T_m) is an important physical parameter that defines the upper temperature limit for the usability of a solid material. A solid exhibiting a higher T_m typically possesses a lower thermal expansion coefficient, greater cohesive and bonding energies, and stronger atomic interactions [36]. Based on the elastic constants, the melting temperature of a material can be estimated through the following empirical relation [37]:

$$T_m = 354 + 1.5(2C_{11} + C_{33}) \tag{7}$$

The elevated Debye temperature also suggests a lower phonon scattering rate and, consequently, enhanced thermal stability. Moreover, its high melting temperature (T_m = 749.74 K) further confirms the superior thermal resistance of $LiMg_2H_5$ under elevated temperatures. In contrast, $NaMg_2H_5$ exhibits the lowest Debye temperature (547.98 K) and sound velocities, reflecting a softer lattice and weaker interatomic interactions. This behavior can be attributed to the larger ionic radius of Na compared to Li, which expands the lattice and reduces the bond strength. Accordingly, $NaMg_2H_5$ displays the lowest melting point

Table 8
Calculated thermophysical parameters including density (ρ), transverse (v_t), longitudinal (v_l), and average (v_m) sound velocities, melting temperature (T_m), Debye temperature (θ_D), minimum thermal conductivity (K_{min}), and Grüneisen parameter (γ_a) for $LiMg_2H_5$, $NaMg_2H_5$, and KMg_2H_5 compounds.

Compound	P (g/cm^3)	v_t (m/s)	v_l (m/s)	v_m (m/s)	T_m (K)	θ_D (K)	K_{min} Wm^{-1} K^{-1}	γ_a
$LiMg_2H_5$	1.25	5312.19	8596.23	5859.01	749.74	807.62	1.73	1.25
$NaMg_2H_5$	1.41	3717.94	6398.66	4125.29	677.42	547.98	1.13	1.47
KMg_2H_5	1.57	4126.84	6789.54	4559.42	690.65	588.16	1.18	1.31

(677.42 K) among the series, indicating relatively lower thermal robustness. The KMg_2H_5 compound shows intermediate characteristics, with a Debye temperature of 588.16 K and an average sound velocity of 4559.42 m/s. Although its density (1.57 g/cm^3) is the highest, suggesting heavier atomic packing, the lower Debye temperature and moderate melting point (690.65 K) imply that the increased atomic mass of K contributes to reduced phonon frequencies and lower lattice stiffness.

The minimum thermal conductivity (K_{min}) represents the lower limit of a material's intrinsic lattice thermal conductivity attainable at elevated temperatures. This property is particularly important because it remains unaffected by structural imperfections, impurities, or lattice defects. Clarke proposed the following equation, based on the quasi-harmonic Debye model, to estimate K_{min} under high-temperature conditions [38]:

$$K_{min} = k_B v_m \left(\frac{M}{n\rho N_A}\right)^{-\frac{2}{3}} \tag{8}$$

The minimum thermal conductivity (K_{min}) values follow the trend $LiMg_2H_5$ (1.73 W/m·K) > KMg_2H_5 (1.18 W/m·K) > $NaMg_2H_5$ (1.13 W/m·K), which aligns with the variation in the Debye temperatures and average sound velocities. This correlation demonstrates that phonon-mediated heat transfer is more efficient in Li-containing hydrides, whereas heavier alkali elements reduce the phonon transport capability.

Additionally, the Grüneisen parameter (γ), which characterizes anharmonic effects and thermal expansion, ranges from 1.25 to 1.47. The following equation can be used to estimate the Grüneisen parameter of XMg_2H_5 (X = Li, Na, K) using acoustic velocities [39]:

$$\gamma_a = \frac{3}{2}\left(\frac{(3v_l^2 - 4v_t^2)}{v_l^2 + 2v_t^2}\right) \tag{9}$$

The lowest γ value for $LiMg_2H_5$ indicates minimal lattice anharmonicity and greater structural stability, while higher γ values for $NaMg_2H_5$ and KMg_2H_5 signify stronger phonon–phonon interactions, leading to increased lattice vibrations and lower thermal conductivity.

Overall, these results suggest that $LiMg_2H_5$ exhibits superior thermophysical performance, with enhanced thermal stability, stronger bonding, and better heat transport behavior, making it a promising candidate for hydrogen storage applications under varying thermal conditions. In contrast, Na- and K-substituted hydrides show progressively softer and more anharmonic lattices, which may influence their hydrogen desorption kinetics and structural stability at high temperatures.

3.6. Hydrogen storage properties

The transition toward sustainable energy systems necessitates the replacement of carbon-based fuels with environmentally friendly alternatives, and hydrogen is widely regarded as a promising clean energy carrier. However, developing materials capable of storing hydrogen efficiently and safely remains one of the main technological challenges. Solid-state hydrogen storage systems, particularly metal hydrides, have gained significant attention due to their high energy density, low operation pressure, and enhanced safety characteristics compared to compressed or liquid hydrogen methods. Among them, perovskite-type and complex hydrides have attracted interest owing to their favorable hydrogen sorption kinetics and high reversible capacity. In this study, the hydrogen storage performance of $LiMg_2H_5$, $NaMg_2H_5$, and KMg_2H_5 compounds was systematically evaluated in terms of desorption temperature (T_{des}), gravimetric capacity (Cwt%), and volumetric capacity (C_v). The obtained results reveal that both the hydrogen content and behavior of description are strongly influenced by the choice of alkali metal. To measure the gravimetric hydrogen content, we use the following equation [40]:

$$C_{wt\%} = \left(\frac{\left(\frac{H}{M}\right)M_H}{M_{Host} + \left(\frac{H}{M}\right)M_H}\, x\, 100\right)\% \tag{10}$$

As shown in Table 9, $LiMg_2H_5$ exhibits the highest gravimetric hydrogen storage capacity of 8.32 wt% and a volumetric capacity of 102.97 gH_2L^{-1}, followed by $NaMg_2H_5$ with 6.58 wt% and 92.16 gH_2L^{-1}, and KMg_2H_5 with 5.43 wt% and 84.40 gH_2L^{-1}, respectively.

The superior performance of $LiMg_2H_5$ is attributed to the smaller ionic radius of Li^+, which promotes denser hydrogen packing and stronger metal–hydrogen interactions. All investigated materials surpass the U.S. Department of Energy (DOE) 2025 target of 5.5 wt% for gravimetric capacity, confirming their potential for practical hydrogen storage applications. The desorption temperature (T_{des}) is another key factor determining the usability of a storage material [41].

The hydrogen desorption characteristics of XMg_2H_5 (X = Li, Na, K) compounds were determined by considering a specific reaction pathway where the complex hydride decomposes into an alkali hydride, metallic magnesium, and molecular hydrogen ($XMg_2H_5 \rightarrow XH + 2\,Mg + 2H_2$). Based on this decomposition route, the calculated desorption temperatures (T_{des}) are 235.82 K for $LiMg_2H_5$, 334.23 K for $NaMg_2H_5$, and 267.74 K for KMg_2H5. These values provide a realistic assessment of the thermal energy required for hydrogen release under practical conditions. Specifically, the desorption temperature of 334.23 K for $NaMg_2H_5$ is particularly noteworthy for solid-state storage applications, as it operates slightly above ambient temperature, enabling controlled hydrogen delivery. Despite the formation of the XH intermediate phase, the gravimetric storage capacities remain high at 8.32 wt%, 6.58 wt%, and 5.43 wt% for the Li, Na, and K-based systems, respectively, with $LiMg_2H_5$ and $NaMg_2H_5$ successfully meeting the DOE 2025 targets.

3.7. Phonon (vibrational) properties

Phonon properties play a central role in evaluating the dynamic stability and hydrogen-related behavior of solid-state hydrogen storage materials. In systems containing light elements such as hydrogen, vibrational characteristics are significant because hydrogen atoms strongly influence both the stability of the host lattice and the energetics of hydrogen adsorption and release. For this reason, phonon dispersion

Table 9
Theoretical desorption temperature (T_{des}, K), gravimetric capacity ($C_{wt.\%}$), and volumetric capacity (C_v) of XMg_2H_5.

Compound	T_{des}	$C_{wt.\%}$	C_v
$LiMg_2H_5$	235.82	8.32	102.97
$NaMg_2H_5$	334.23	6.58	92.16
KMg_2H_5	267.74	5.43	84.40

relations were calculated to assess the vibrational stability of the investigated structures and to gain deeper insight into their suitability for hydrogen storage applications. As illustrated in Fig. 6(a–c), the phonon dispersion curves of $LiMg_2H_5$, $NaMg_2H_5$, and KMg_2H_5 calculated along the high-symmetry Γ–X–S–Y–Γ path show that all vibrational modes remain positive across the entire Brillouin zone.

The complete absence of imaginary modes confirms that the structures are dynamically stable and do not show any tendency toward lattice instability under small atomic displacements. This result is especially significant for hydrogen storage materials, as dynamic stability is a prerequisite for maintaining structural integrity during hydrogen absorption and desorption processes, which are typically accompanied by thermal fluctuations.

The structures investigated contain 16 atoms per unit cell, resulting in a total of 48 phonon branches, in accordance with the 3 N rule. Among these, three branches correspond to acoustic modes, while the remaining 45 branches are optical modes. The acoustic phonon branches originate smoothly from zero frequency at the Γ point, reflecting the collective, in-phase motion of atoms within the lattice and confirming the mechanical consistency of the crystal structures. These modes are closely related to the elastic response of the material and provide indirect insight into its mechanical robustness. The large number of optical phonon modes observed at higher frequencies is a direct consequence of the multi-atomic unit cell and the presence of hydrogen atoms. Due to their low atomic mass, hydrogen atoms contribute predominantly to high-frequency vibrational modes, which are clearly visible in the phonon spectra. These high-frequency optical modes indicate strong and directional metal–hydrogen interactions, suggesting that hydrogen is firmly bound within the crystal framework. Such vibrational behavior is generally associated with good hydrogen retention and reduced risk of premature hydrogen release under ambient conditions.

From a hydrogen storage perspective, the distribution of phonon modes provides valuable information about both thermal stability and desorption behavior. The absence of soft modes at low frequencies suggests that the lattice remains stable upon thermal excitation, while the well-separated high-frequency hydrogen-related optical modes point to a balanced binding strength. This balance is essential for practical hydrogen storage, as excessively weak bonding would lead to hydrogen loss, whereas overly strong bonding could result in unacceptably high desorption temperatures. Furthermore, the smooth dispersion of both acoustic and low-frequency optical modes indicates a well-ordered vibrational landscape, which is favorable for reversible hydrogen diffusion within the lattice. Such vibrational characteristics imply that hydrogen atoms can migrate in a controlled manner without triggering structural degradation, an important requirement for long-term cycling stability. Overall, the phonon dispersion results demonstrate that the materials investigated are vibrationally and dynamically stable, with phonon features that are well aligned with the key requirements for efficient and reversible hydrogen storage.

4. Conclusion

In this study, we present a detailed first-principles analysis of the structural, elastic, electronic, vibrational, thermodynamic, and hydrogen storage characteristics of orthorhombic XMg_2H_5 (X = Li, Na, K) hydrides. The calculated negative formation energies indicate that all compounds are thermodynamically stable in the *Pmmn* phase, suggesting that their experimental synthesis is feasible. Among the investigated systems, $LiMg_2H_5$ stands out due to its compact crystal structure, the highest bulk and shear moduli, and the largest Debye temperature, indicating strong interatomic interactions and enhanced mechanical and thermal robustness. By comparison, $NaMg_2H_5$ exhibits lower stiffness together with pronounced elastic anisotropy, underscoring the directional nature of its mechanical response, whereas KMg_2H_5 shows intermediate rigidity accompanied by improved machinability. Despite these differences, all compounds are predicted to be intrinsically brittle, a behavior commonly observed in complex metal hydrides.

The electronic properties further reveal that all XMg_2H_5 compounds are wide-band-gap semiconductors, with hydrogen-derived states playing a dominant role near both the valence and conduction band edges. This electronic structure reflects a predominantly ionic bonding character, which is advantageous for reversible hydrogen storage. Consistent with these findings, optical calculations identify strong interband transitions in the ultraviolet region and plasmon resonance features in the 9–12 eV energy range, offering distinct spectroscopic fingerprints that could be used to monitor hydrogenation and dehydrogenation

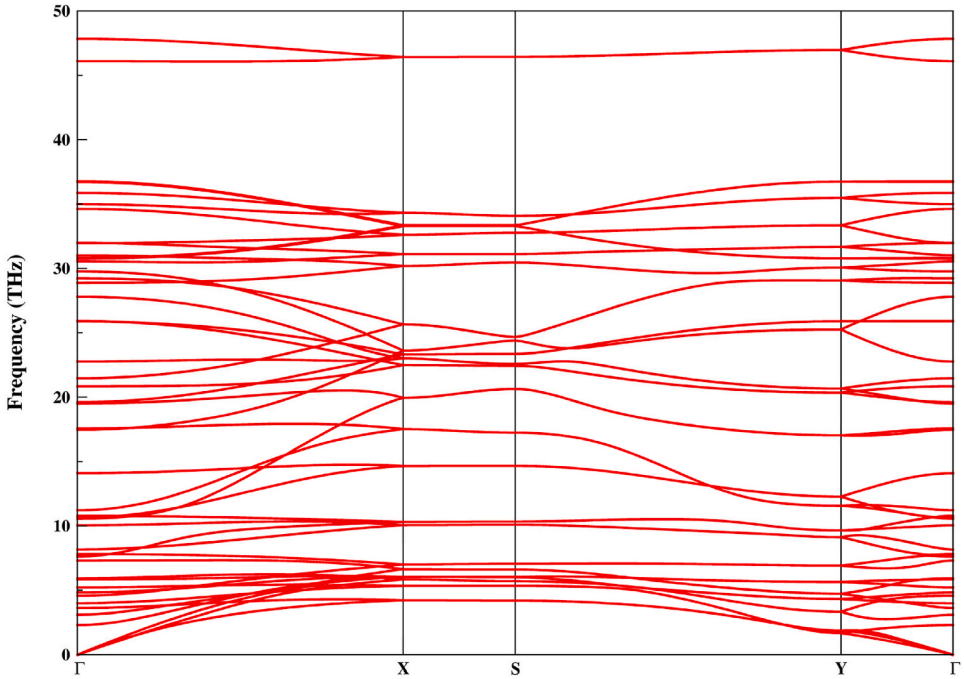

Fig. 6(a). The phonon dispersion curves for $LiMg_2H_5$.

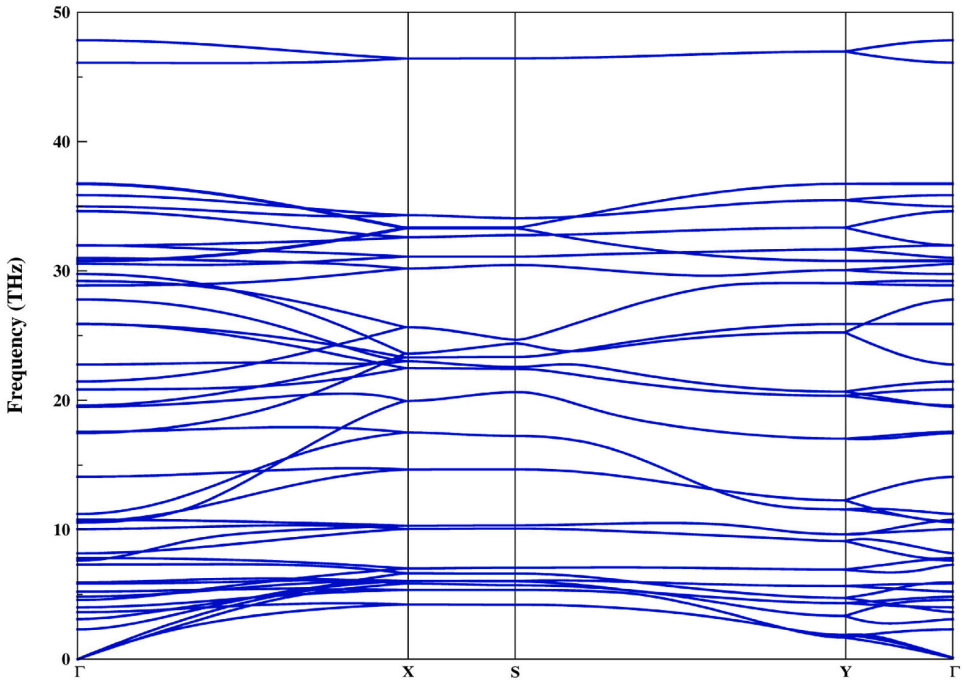

Fig. 6(b). The phonon dispersion curves for $NaMg_2H_5$.

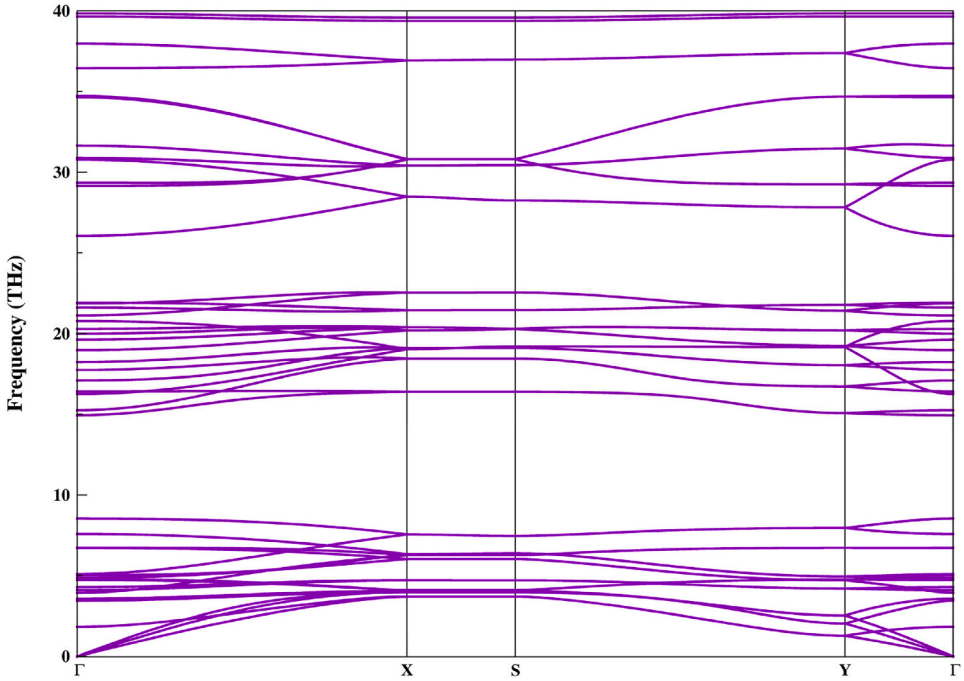

Fig. 6(c). The phonon dispersion curves for KMg_2H_5.

processes. To evaluate lattice dynamics and structural robustness, phonon dispersion calculations were also carried out for all XMg_2H_5 systems. The complete absence of imaginary phonon frequencies across the Brillouin zone confirms that $LiMg_2H_5$, $NaMg_2H_5$, and KMg_2H_5 are dynamically stable in the orthorhombic *Pmmn* structure. This result lends additional confidence to the predicted physical properties and supports the suitability of these hydrides for practical applications.

From the perspective of hydrogen storage performance, $LiMg_2H_5$ provides the highest gravimetric (8.32 wt%) and volumetric hydrogen capacities, surpassing the U.S. DOE 2025 target, while $NaMg_2H_5$ is distinguished by its lower hydrogen desorption temperature, indicative of easier hydrogen release. Taken together, these results highlight a clear trade-off between storage capacity, thermal stability, and desorption behavior that can be systematically tuned through alkali-metal substitution.

CRediT authorship contribution statement

Salih Ermiş: Writing – review & editing, Writing – original draft, Investigation. **Sümeyra Yamçıçıer:** Writing – review & editing, Writing

– original draft, Methodology, Conceptualization. **Cihan Kürkçü:** Writing – review & editing, Writing – original draft, Methodology, Investigation, Funding acquisition.

Declaration of generative AI and AI-assisted technologies in the writing process

During the preparation of this work, the author(s) used an artificial intelligence tool to improve the language and readability of the study. After using this tool/service, the author(s) reviewed and edited the content as needed and took(s) full responsibility for the content of the publication.

Declaration of competing interest

The authors declare that they have no known competing financial interests or personal relationships that could have appeared to influence the work reported in this paper.

Acknowledgment

This study was supported by the Kırşehir Ahi Evran University under the Scientific Research Project No: TBY.A1.24.001.

References

[1] Turner JA. Sustainable hydrogen production. Science 2004;305:972–4.
[2] Züttel A. Materials for hydrogen storage. Mater Today 2003;6:24–33.
[3] Schlapbach L, Züttel A. Hydrogen-storage materials for mobile applications. Nature 2001;414:353–8.
[4] Yamçıçıer Ç, Yamçıçıer S, Kürkçü C. AI-driven discovery of high-performance LiMHx (M= Sc, Ti; x= 3, 4, 5) hydrides: a first-principles investigation structural, mechanical, electronic, thermophysical, optical and hydrogen storage properties. Int J Hydrogen Energy 2025;187:152097.
[5] Ermiş S, İyigör A, Kürkçü C. Investigation of K2TiH6 and Ca2TiH6 under pressures from 0 to 20 GPa: structural, electronic, thermodynamic, mechanical, vibrational, and hydrogen storage properties. Int J Hydrogen Energy 2025;177:151653.
[6] Jain I, Lal C, Jain A. Hydrogen storage in Mg: a most promising material. Int J Hydrogen Energy 2010;35:5133–44.
[7] Yamçıçıer Ç, Kürkçü C. Structural, elastic, optic, electronic, phonon, thermodynamic, and hydrogen storage properties of bialkali alanates M2LiAlH6 (M= Na, K). Int J Hydrogen Energy 2025;135:440–56.
[8] Liu C, Li F, Ma LP, Cheng HM. Advanced materials for energy storage. Adv Mater 2010;22:E28–62.
[9] Sakintuna B, Lamari-Darkrim F, Hirscher M. Metal hydride materials for solid hydrogen storage: a review. Int J Hydrogen Energy 2007;32:1121–40.
[10] Beyazit Nİ. Comparative study of hydrogen storage and metal hydride systems: future energy storage solutions. Processes 2025;13:1506.
[11] Liang G, Huot J, Boily S, Van Neste A, Schulz R. Hydrogen storage properties of the mechanically milled MgH2–V nanocomposite. J Alloys Compd 1999;291:295–9.
[12] de Jongh PE, Adelhelm P. Nanosizing and nanoconfinement: new strategies towards meeting hydrogen storage goals. ChemSusChem 2010;3:1332–48.
[13] Yamçıçıer Ç. Exploring the structural, elastic, phonon, optoelectronics, and thermoelectric properties of tetragonal complex metal hydride X2MgH4 (X= K, Rb, and Cs) compounds for hydrogen storage applications. Int J Hydrogen Energy 2023;48:39930–43.
[14] Ren L, Li Y, Zhang N, Li Z, Lin X, Zhu W, et al. Nanostructuring of Mg-based hydrogen storage materials: recent advances for promoting key applications. Nano-Micro Lett 2023;15:93.
[15] Gbenebor OP, Popoola API. Transition metal-based materials and their catalytic influence on MgH2 hydrogen storage: a review. Int J Renew Energy Dev 2023;12:1141–59.
[16] Yang J, Sudik A, Wolverton C, Siegel DJ. High capacity hydrogen storage materials: attributes for automotive applications and techniques for materials discovery. Chem Soc Rev 2010;39:656–75.
[17] Orimo S-i, Nakamori Y, Eliseo JR, Züttel A, Jensen CM. Complex hydrides for hydrogen storage. Chem Rev 2007;107:4111–32.
[18] Łodziana Z, Vegge T. Structural stability of complex hydrides: l i BH 4 revisited. Phys Rev Lett 2004;93:145501.
[19] Ohba N, Miwa K, Aoki M, Noritake T, Towata S-i, Nakamori Y, et al. First-principles study on the stability of intermediate compounds of LiBH 4. Phys Rev B Condens Matter 2006;74:075110.
[20] Michel KJ, Akbarzadeh AR, Ozolins V. First-Principles study of the li– Mg– N– H system: compound structures and hydrogen-storage properties. J Phys Chem C 2009;113:14551–8.
[21] Pottmaier Vicente D, Baricco M. Materials for hydrogen storage and the Na-Mg-BH system. AIMS Energy 2015;3:75–100.
[22] Bhihi M, El Khatabi M, Lakhal M, Naji S, Labrim H, Benyoussef A, et al. First principle study of hydrogen storage in doubly substituted Mg based hydrides. Int J Hydrogen Energy 2015;40:8356–61.
[23] Baran A, Polański M. Magnesium-based materials for hydrogen storage—a scope review. Materials 2020;13:3993.
[24] Abdellaoui M, Lakhal M, Bhihi M, El Khatabi M, Benyoussef A, El Kenz A, et al. First principle study of hydrogen storage in doubly substituted Mg based hydrides Mg5MH12 (M= B, Li) and Mg4BLiH12. Int J Hydrogen Energy 2016;41:20908–13.
[25] Gao P, Zhang X, Hu X, Yu X, Sun D, Fang F, et al. Li/Mg-Based hydrides for high-capacity hydrogen and lithium storage applications. Adv Funct Mater 2025:2425155.
[26] Moharam M, Saleh EAM, Sabeen S, Hussain K, Alshik NM, Nabil G, et al. Multifaceted exploration of structural, optoelectronic, mechanical, bader charge, phononic, and hydrogen storage properties of novel Li-based hydrides for energy applications. Int J Hydrogen Energy 2025;117:300–13.
[27] Hirscher M, Yartys VA, Baricco M, von Colbe JB, Blanchard D, Bowman Jr RC, et al. Materials for hydrogen-based energy storage–past, recent progress and future outlook. J Alloys Compd 2020;827:153548.
[28] Clark SJ, Segall MD, Pickard CJ, Hasnip PJ, Probert MI, Refson K, et al. First principles methods using CASTEP. Z Kristallogr Cryst Mater 2005;220:567–70.
[29] Perdew JP, Burke K, Ernzerhof M. Generalized gradient approximation made simple. Phys Rev Lett 1996;77:3865.
[30] Fischer TH, Almlof J. General methods for geometry and wave function optimization. J Phys Chem 1992;96:9768–74.
[31] Monkhorst HJ, Pack JD. Special points for Brillouin-zone integrations. Phys Rev B 1976;13:5188.
[32] Momma K, Izumi F. VESTA: a three-dimensional visualization system for electronic and structural analysis. Applied Crystallography 2008;41:653–8.
[33] Mouhat F, Coudert F-X. Necessary and sufficient elastic stability conditions in various crystal systems. Phys Rev B 2014;90:224104.
[34] Anderson OL. A simplified method for calculating the debye temperature from elastic constants. J Phys Chem Solid 1963;24:909–17.
[35] Schreiber E, Anderson OL, Soga N, Bell JF. Elastic constants and their measurement. 1975.
[36] Fine M, Brown L, Marcus H. Elastic constants versus melting temperature in metals. Scripta Metall 1984;18:951–6.
[37] Clarke D. Communicative intent and conventionality. Sign levels: language and its evolutionary antecedents. Springer; 2003. p. 67–93.
[38] Clarke DR. Materials selection guidelines for low thermal conductivity thermal barrier coatings. Surf Coating Technol 2003;163:67–74.
[39] Arab F, Sahraoui FA, Haddadi K, Bouhemadou A, Louail L. Phase stability, mechanical and thermodynamic properties of orthorhombic and trigonal MgSiN2: an ab initio study. Phase Transitions 2016;89:480–513.
[40] Pluengphon P, Tsuppayakorn-aek P, Sukmas W, Inceesungvorn B, Bovornratanaraks T. Dynamical stabilization and H-vacancy diffusion kinetics of lightweight complex hydrides: ab initio study for hydrogen storage improvement. Int J Hydrogen Energy 2021;46:22591–8.
[41] Zeng Q, Su K, Zhang L, Xu Y, Cheng L, Yan X. Evaluation of the thermodynamic data of CH3SiCl3 based on quantum chemistry calculations. J Phys Chem Ref Data 2006;35:1385–90.